Editors' Suggestion

Nonlinear Coupling Induced Anomalous State Transfer and Complete Multistate Excitation via Adiabatic Control

Zhao-Xian Chen,[1,2,*] Yi Ru,[1,*] Guang-Chen He,[1] Ming-Hui Lu,[1,2] Yan-Feng Chen,[2] Yan-Qing Lu,[2,†] and Ze-Guo Chen[1,‡]

[1]School of Materials Science and Intelligent Engineering, Nanjing University, Suzhou, 215163, China
[2]National Laboratory of Solid State Microstructures, College of Engineering and Applied Sciences, and Collaborative Innovation Center of Advanced Microstructures, Nanjing University, Nanjing, 210023, China

(Received 4 September 2025; revised 10 November 2025; accepted 20 November 2025; published 20 January 2026)

We theoretically proposed and experimentally demonstrated that a nonlinear acoustic dimer system with amplitude-dependent and sign-reversible coupling exhibits unprecedented control over multistability and state selection. The engineered inter-resonator coupling $\kappa = \kappa_0 + \alpha|\psi_1|^2$ yields a quintic steady-state response with at most three dynamically stable states: low (LS), intermediate (IS), and high (HS). Monotonic sweeps produce asymmetric hysteresis—LS → HS on upsweep, but HS → IS → LS on downsweep—leaving a linearly stable yet dynamically inaccessible IS under conventional driving. Basin-of-attraction analysis shows that nonlinear coupling reshapes the phase-space geometry, creating barriers that isolate the IS. Leveraging this insight, we developed a simple up-down-up adiabatic protocol that achieves full and selective access to all stable states, including the otherwise transparent IS. Mapping versus drive frequency and damping reveals transitions from separated bistable loops to a unified tristable regime. These results, to our knowledge, provide the first experimental realization of nonlinear-coupling-governed multistability and a versatile route to programmable multistate control.

DOI: 10.1103/6bsr-x2v9

Introduction—Nonlinear systems display a rich variety of phenomena—solitons, chaos, multistability, and pattern formation—that are foundational across modern physics [1–3]. Multistability, where multiple stable states coexist under identical parameters, underpins dynamics in diverse areas of physics [4–9], biology [10–12], engineering [13–16], and ecology [17,18]. Transfers between these states, often characterized by hysteresis under adiabatic driving, typically proceed sequentially between adjacent energy levels. For example, in a driven-dissipative system, one commonly observes switching from a low-amplitude state (LS) to a high-amplitude state (HS) as the driving strength increases, as the system can absorb and store more energy from the external source. However, interacting nonlinear systems can harbor intermediate states (IS) that are linearly stable yet dynamically inaccessible—folded inside the hysteresis loops and missed by conventional protocols [19–21]. Recent advances have proposed pulse excitations as a route to unfold such hidden IS [21], opening avenues for information encryption and dynamic control, yet still experimentally elusive.

A fundamental question emerges: how can a linearly stable IS remain dynamically inaccessible under conventional driving? While recent studies have shown that utilizing onsite nonlinearity can excite such hidden IS, these approaches typically rely on pulse excitations or fine-tuned initializations, offering limited insight into the general accessibility criteria [21]. Here, we reveal that nonlinear coupling—a distinct mechanism from onsite nonlinearity—can reshape the attractor landscape to form topological barriers, dynamically isolating the IS despite its linear stability. This leads to the emergence of "transparent" IS during LS → HS transfers, unreachable under standard adiabatic sweeps. Such insights go beyond specific models, offering a general framework for understanding multistability in driven nonlinear systems.

To demonstrate this, we propose a dimer system with programmable nonlinear coupling $\kappa = \kappa_0 + \alpha|\psi_1|^2$, where the sign-flipping capability ($\kappa_0 > 0$ and $\alpha < 0$) enables nontrivial attractor topology and unprecedented control over multistability. Distinct from material-based or on-site nonlinearities (e.g., Kerr-type effects in optics) [22–29], nonlinear coupling—where interactions depend on the subsystem amplitudes/phases—has emerged as a distinct paradigm for wave control [30–36], for instance, in inducing the reversal of non-Hermitian skin effects in circuit systems [37]. Here, we provide a general, programmable realization in acoustics with amplitude-dependent, sign-reversible coupling, unlocking precise control of multistability and transfer pathways. The nonlinear coupling induces asymmetric state transfers—LS → HS during upward sweeps and HS → IS → LS during downward

*These authors contributed equally to this work.
†Contact author: yqlu@nju.edu.cn
‡Contact author: zeguoc@nju.edu.cn

sweeps—highlighting the coupling's crucial role in state selection. By combining adiabatic driving with attractor basin engineering, we achieve full state accessibility, including the otherwise "transparent" IS, via a circuitous evolution strategy. Our platform provides the first experimental demonstration of multistability governed by nonlinear coupling, bridging theoretical concepts with physical realizations.

Nonlinear coupling system for tristability—To explore how nonlinear inter-resonator coupling can give rise to multistable dynamics, we consider a minimal system composed of two coupled resonators, as schematically illustrated in Fig. 1(a). In typical experimental or simulation settings, the system is driven by exciting one of the resonators and observing how its response evolves with respect to varying driving parameters. Here, without loss of generality, we consider that Resonator 1 is driven by a harmonic source of frequency f_{in} and amplitude A_{in}. Crucially, the coupling strength κ between the two resonators is not constant, but depends nonlinearly on the field intensity inside Resonator 1 $|\psi_1|$, i.e., $\kappa = \kappa_0 + \alpha|\psi_1|^2$, where $\kappa_0 > 0$ is the baseline coupling and $\alpha < 0$ introduces amplitude-dependent weakening and eventual sign reversal

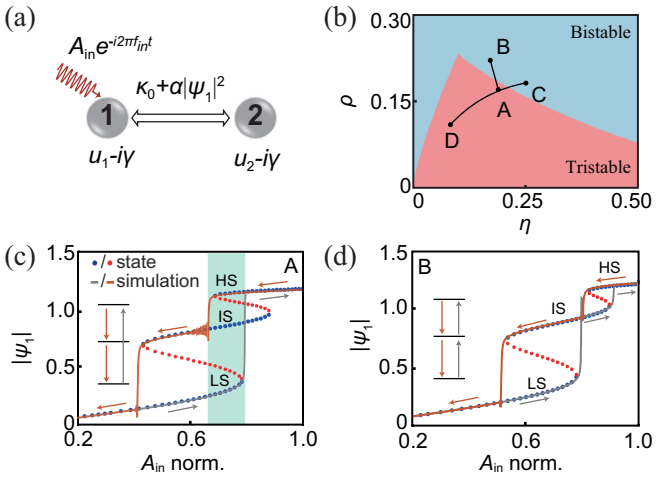

FIG. 1. Nonlinear coupled resonator system and multistable characteristics. (a) Schematic of two resonators with amplitude-dependent nonlinear coupling $\kappa = \kappa_0 + \alpha|\psi_1|^2$, where $|\psi_1|$ is the wave amplitude in Resonator 1. The system parameters include resonant frequencies $u_{1,2}$, damping rate γ, and external drive (frequency f_{in} and amplitude A_{in}). (b) Phase diagram showing bistable (blue) and tristable (red) regions in $[\eta, \rho]$ parameter space, with representative points A, D (tristable) and B, C (bistable) marked. (c) Tristable response for case A $[\eta, \rho] = [0.181, 0.162]$. Calculated stable states (LS/IS/HS, blue dots) and unstable solution (red) versus normalized A_{in}, with the tristable state range marked in green. Gray/orange curves show simulated hysteresis loops during A_{in} sweep up/sweep down, revealing counterintuitive and asymmetric transfers between LS and HS, as schematically illustrated in the inset. (d) Corresponding bistable behavior for case B $[\eta, \rho] = [0.163, 0.215]$, exhibiting separated hysteresis loops and sequential state transfers (see the inset).

of the coupling when $|\psi_1|$ exceeds $\sqrt{\kappa_0/|\alpha|}$. This form of nonlinear coupling enables qualitatively distinct multistability scenarios compared to conventional Kerr-type systems. The system dynamics are governed by

$$i\frac{\mathrm{d}}{\mathrm{d}t}\Psi = 2\pi\begin{bmatrix} u_1 - i\gamma & \kappa \\ \kappa & u_2 - i\gamma \end{bmatrix}\Psi + 2\pi\begin{bmatrix} 1 \\ 0 \end{bmatrix}s, \quad (1)$$

where $u_{1,2}$ and γ, respectively, denote the resonant frequency and damping factor of the cavities, $s = A_{\mathrm{in}}\mathrm{e}^{-2\pi i f_{\mathrm{in}}t}$ is the source signal, and $\Psi = [\psi_1, \psi_2]^{\mathrm{T}}$ represents complex wave functions of the physical system, e.g., acoustic pressure fields inside the cavities experimentally investigated later. Equation (1) takes the form of a driven-dissipative Schrödinger-type equation, a standard framework for modeling coupled classical wave systems [38–40]. To analyze the steady-state response, we seek solutions of the form $\psi_{1,2}(t) = A_{1,2}e^{-i\theta_{1,2}}e^{-2\pi i f_{\mathrm{in}}t}$, and substitute them into the coupled-mode equations. This yields a real algebraic equation for the rescaled intensity variable $\tilde{I}_1 = \alpha A_1^2/\kappa_0$, whose explicit form is a quintic polynomial,

$$\tilde{I}_1^5 + 4\tilde{I}_1^4 - 2(\eta - 3)\tilde{I}_1^3 - 4(\eta - 1)\tilde{I}_1^2 + [(\eta - 1)^2 + \rho^2]\tilde{I}_1 - \Omega = 0, \quad (2)$$

where the dimensionless parameters $\eta = (\Gamma_1\Gamma_2 - \gamma^2)/\kappa_0^2$, $\rho = (\Gamma_1 + \Gamma_2)\gamma/\kappa_0^2$, and $\Omega = \alpha A_{\mathrm{in}}^2(\Gamma_2^2 + \gamma^2)/\kappa_0^5$ encode the detuning and drive strength, with $\Gamma_{1,2} = u_{1,2} - f_{\mathrm{in}}$ (see the derivations in [40]). We note that while the polynomial is of fifth order and can in principle admit up to five real negative roots (corresponding to possible stationary amplitudes), not all of them are dynamically stable. In fact, the Routh–Hurwitz analysis [43] constrains the number of dynamically stable fixed points to no more than three [40]. These stable solutions correspond to the coexisting low, intermediate, and high amplitude states (LS, IS, and HS), forming the basis of tristability. We emphasize that the nonlinear coupling, while depending solely on the wave amplitude in Resonator 1, is mutual and reciprocal, which is sufficient for the emergence of multistability [40].

To assess the emergence of tristability, we construct a phase diagram using the dimensionless parameters η and ρ, which are determined by the system's intrinsic properties. At a fixed driving frequency, these parameters remain constant, while the drive-dependent term Ω varies with the input amplitude. This allows us to treat η and ρ as coordinates, and determine whether tuning the input strength can induce three coexisting stable states. As shown in Fig. 1(b), the red region indicates parameter combinations where tristability is possible over a finite range of drive amplitudes. For example, point A with $[\eta, \rho] = [0.181, 0.162]$ lies in the tristable region. Within a finite range of input amplitude A_{in} [marked in green in Fig. 1(c)], Eq. (2) yields five real positive solutions for $|\psi_1|$, among

which three are dynamically stable—corresponding to the LS, IS and HS, respectively. Interestingly, adiabatic modulation of A_{in} reveals an asymmetric transfer pathway: during upward sweeps (gray curve), the system remains in LS until a bifurcation point is reached, where it directly jumps to HS while bypassing the stable IS. In contrast, downward sweeps (orange curve) result in a sequential HS → IS → LS transfer. This directional asymmetry is a hallmark of our coupling-induced mechanism, which reshapes the underlying basins of attraction—allowing LS to be dynamically engulfed by HS during the upward sweep, while preserving IS accessibility in the reverse direction. In bistable regions [e.g., point B with $[\eta, \rho] = [0.163, 0.215]$ in Fig. 1(b)], the system exhibits two disconnected hysteresis loops involving IS and either LS or HS, as shown in Fig. 1(d). This fragmented bistability landscape further underscores the role of nonlinear coupling in sculpting unconventional state selection rules. Such asymmetry in transfer pathways stands in stark contrast to standard nonlinear systems, where multistability typically yields symmetric hysteresis loops and predictable bifurcation cascades [21]. These state-selection pathways are examined and verified experimentally in the following sections.

Acoustic realization of nonlinear coupling—Nonlinear coupling, in which the interaction itself depends on local state variables, has only recently begun to be explored and remains uncommon in controlled experiments. To experimentally realize the predicted tristable dynamics governed by nonlinear inter-resonator coupling, we construct an active acoustic system that emulates Schrödinger-type dynamics using gain-controlled feedback circuits [39,44–49]. As illustrated in Fig. 2(a), the system comprises two cuboid acoustic resonators, each embedded with a speaker and a microphone, calibrated to have slightly detuned natural frequencies at $u_1 = 1725.3$ Hz and $u_2 = 1729$ Hz. In-phase feedback loops (red lines) are implemented to compensate for intrinsic losses, tuning the effective damping to $\gamma = 1$ Hz in both resonators.

The core of our design lies in the coupling path (blue lines), where a signal processor modulates the inter-resonator coupling according to the wave amplitude, thus encoding a nonlinear coupling $\kappa(|\psi|^2)$. Specifically, the processor is programmed with a transfer function $p_{\mathrm{out}} = (1+\alpha|p_c|^2/\kappa_0)p_{\mathrm{in}}$, where $\kappa_0 = 6.7$ Hz and $\alpha = -8.3$ HzPa^{-2}. Here, p_{in} and p_{out} denote the input and output signals along the coupling path, and p_c is a control signal. Finally, we close the loop by feeding back the local pressure signal p_1 as the control input p_c, thereby establishing a self-regulating, amplitude-sensitive coupling pathway. By externally controlling p_c and sweeping the excitation frequency, we measure the pressure response p_2, presented in Fig. 2(b), which exhibits strong agreement with coupled-mode theory predictions [40]. As shown in Fig. 2(c), the extracted coupling strength κ follows the anticipated form

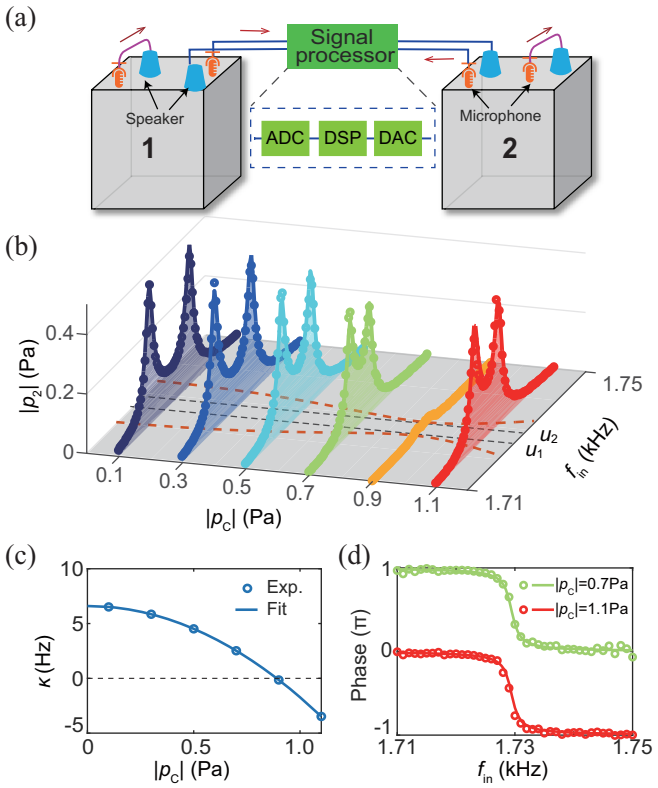

FIG. 2. Experimental realization of nonlinear coupling in acoustic resonators. (a) Schematic of the acoustic implementation using two coupled cavities with active feedback circuits. In-phase compensation circuits (red) balance cavity damping, while programmable coupling circuits (blue) implement the nonlinear coupling via a signal processor, which includes an analog-to-digital converters (ADC), a digital signal processor (DPS) core, and a digital-to-analog converter (DAC). Signal directions are denoted with red arrows. Microphones and speakers enable wave excitation and detection. Other elements, including phase shifters and amplifiers, are omitted for clarity. (b) Measured (circles) and fitted (curves) pressure responses $|p_2|$ as a function of control pressure $|p_c|$ and driving frequency f_{in}. The brown dashed curves indicate the peak positions, while the black dashed lines indicate the resonant frequencies u_1 and u_2 of the two isolated cavities. (c) Extracted κ values (circles) follow the predicted quadratic dependence $\kappa = \kappa_0 + \alpha|p_c|^2$ (curves), demonstrating sign reversal ($\kappa < 0$) above $|p_c| = 0.89$ Pa. (d) Measured (circles) and fitted (curves) $\mathrm{Arg}(p_2/p_1)$, consistent with κ's positive or negative nature with $|p_c|$ set as 0.7 (green) or 1.1 Pa (red), respectively.

$\kappa_0 + \alpha|p_c|^2$, transitioning from positive to negative values when $|p_c| > 0.89$ Pa. This sign reversal is further validated by a π-phase jump in $\mathrm{Arg}(p_2/p_1)$ shown in Fig. 2(d). This experimental platform thus realizes, to our knowledge, the first demonstration of amplitude-dependent, sign-reversible inter-resonator coupling in an acoustic system. The introduction of the signal process makes it more programmable and reversible compared with other physical systems [50,51].

Full tristability access via adiabatic control—We experimentally verify the asymmetric hysteresis predicted in

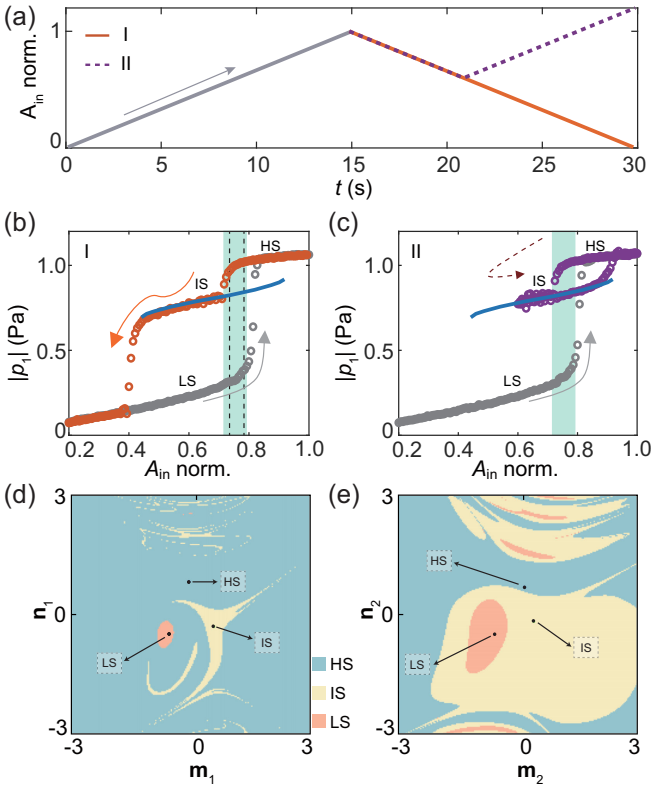

FIG. 3. Controlled excitation of multistable states through tailored driving protocols. (a) Two modulation schemes for the driving amplitude A_{in}: linear ramp-up followed by linear decay (I) and up-down-up linear modulation (II). The source frequency is set as $f_{\mathrm{in}} = 1723.6$ Hz. (b) State transfers under Scheme I: experimental measurements (circles) reveal direct LS → HS jump during ramp up (gray), followed by sequential HS → IS → LS transfers during ramp down (orange). Blue curves denote theoretically predicted intermediate states, with the green region marking the tristable parameter range. (c) State transfers via Scheme II: the up-down-up modulation enables full exploration of IS branches within the tristable region that are inaccessible through simple ramp protocols. (d),(e) Basins of attraction for $A_{\mathrm{in}} = 0.78$ (d) and $A_{\mathrm{in}} = 0.69$ (e), denoted with dashed lines in (b). Each plot shows a cross section in the plane defined by the three stable states (black dots), spanned by $[\mathbf{m}, \mathbf{n}]$ (see details in Supplemental Material [40]), where $\mathbf{m}_1 = [-0.89, -0.29, 0.35, 0.011]^{\mathrm{T}}$, $\mathbf{n}_1 = [0.36, -0.66, 0.34, -0.56]^{\mathrm{T}}$, $\mathbf{m}_2 = [-0.84, -0.40, 0.37, 0.071]^{\mathrm{T}}$, $\mathbf{n}_2 = [0.25, -0.69, -0.040, -0.68]^{\mathrm{T}}$.

Fig. 1(c) by fixing $f_{\mathrm{in}} = 1723.6$ Hz and performing a monotonic sweep of the excitation amplitude A_{in}. Shown as path I in Fig. 3(a), $|dA_{\mathrm{in}}/dt|$ is constant in every linear ramp section, and the total time is set as 30 s to guarantee the adiabaticity [40]. As shown in Fig. 3(b), the system switches from the LS to HS during the up-sweep, but returns only to IS during the down-sweep—confirming the existence of a dynamically inaccessible yet stable intermediate state under standard excitation protocols.

The observed asymmetry prompts an analysis of the attractor landscape shaped by the nonlinear coupling. Each fixed point—LS, IS, and HS—corresponds to a complex state vector $\Psi^{(0)} = (\psi_1^{(0)}, \psi_2^{(0)}) \in \mathbb{C}^2$, forming a three-point configuration embedded in a real four-dimensional space $\mathbb{R}^4$. These states span an affine subspace, which we take as the base plane for computing the basins of attraction. A basin comprises initial conditions that evolve into a given attractor under the system's nonlinear dynamics. Figure 3(d) displays the computed basins at $A_{\mathrm{in}} = 0.78$, revealing that the IS basin is topologically disconnected from LS basin and geometrically adjacent to HS. This explains why the system transfers from LS to HS upon increasing A_{in}—as the attractor LS degenerates, its basin is naturally absorbed by the nearby HS basin, while the IS basin remains inaccessible. Conversely, as $A_{\mathrm{in}} = 0.69$ [Fig. 3(e)] and decreases adiabatically, the HS basin gradually contracts and will be eventually engulfed by that of IS; consequently, the system can subsequently transfer only from HS to IS.

This insight offers a strategy to access the otherwise inaccessible IS. By first increasing A_{in} to enter the HS basin, then decreasing it to fall into IS, and finally re-increasing A_{in} to remain in IS, one can reliably reach the intermediate state [path II in Fig. 3(a)]. The experimental response shown in Fig. 3(c) confirms the success of this protocol, validating the predictive power of the basin geometry. This geometric insight into attraction of basins offers not only an explanation for the observed hysteresis asymmetry, but also a practical handle to engineer and select target states from multistability, which we demonstrate in the following section. Our mechanism relies on quasistatic (adiabatic) modulation of the external drive amplitude to reshape the basins of attraction, whereas onsite-nonlinearity models with amplitude-dependent internal energy input (no external source) achieve state transfer directly via basin selection and thus do not require adiabaticity [29].

Tunable multistate engineering—Our system exhibits exceptional tunability of multistable behavior via multiple parameters, notably the excitation frequency f_{in} and damping rate γ. Using the same A_{in} sweep protocol, we experimentally map the tristable region width $\Delta_{A\mathrm{in}}$ as a function of f_{in} [Fig. 4(a), along path C-D in Fig. 1(b)]. As f_{in} increases, the system evolves from a bistable regime with separated hysteresis loops to a unified tristable regime, as shown in Figs. 4(b) and 4(c), revealing a structure transition in the underlying attractor landscape. We note the LS → HS transfer in Fig. 3(c) differs from that in Fig. 1(c) and is straightforward due to the missing overlap between LS and IS [40].

Tuning the damping rate γ offers another independent knob: at fixed $f_{\mathrm{in}} = 1723.6$ Hz, increasing γ to 1.3 Hz [point B in Fig. 1(b)] suppresses one attractor, recovering bistability shown in Fig. 4(d). These results establish our platform as a versatile and reconfigurable test bed for engineering nonlinear dynamics, with potential implications for programmable acoustic logic and adaptive devices.

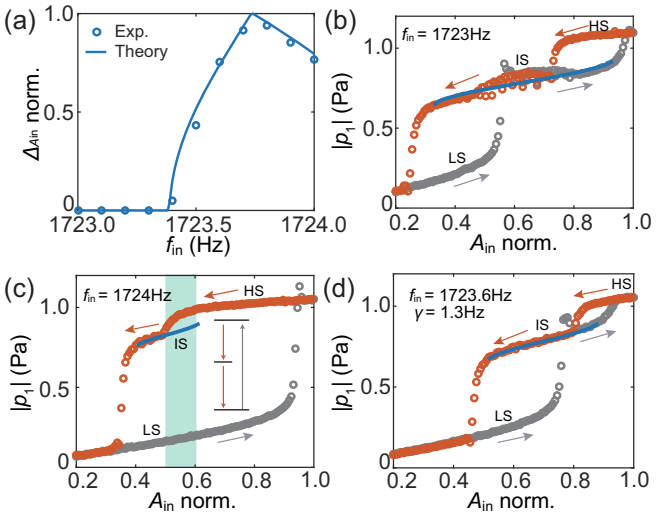

FIG. 4. Frequency- and damping-tuned multistability transfer. (a) Normalized tristable region width Δ_{Ain} versus f_{in}, corresponding to path C-D in Fig. 1(b). $\gamma = 1$ Hz, and maximum of A_{in} is maintained. (b),(c) Experimental state transfers under A_{in} sweeping with $f_{in} = 1723$ Hz (b) and $f_{in} = 1724$ Hz (c). The blue curves denote the calculated IS. The inset in (c) presents the asymmetric state transfers and is different from that in Fig. 1(c). (d) Damping-controlled multistability transfer: with γ increased to 1.3 Hz at fixed $f_{in} = 1723.6$ Hz [case B in Fig. 1(b)], the system reverts to bistable operation, showing separated hysteresis loops similar to (b).

Conclusion and discussion—We have shown that multistability can be engineered and controlled via nonlinear inter-resonator coupling. In a minimal acoustic dimer with programmable coupling $\kappa = \kappa_0 + \alpha|\psi_1|^2$, we observed asymmetric hysteresis—LS → HS on upsweep but HS → IS → LS on downsweep. Basin-of-attraction analysis reveals why an explicit IS remains dynamically inaccessible under monotonic drives and explains the failure of conventional pulse-excitation methods for LS → IS transfers (see Sec. 1.6 in [40]). This understanding enabled our development of a simple up-down-up protocol that reliably accesses all states, including the normally "transparent" IS. The actively tuned acoustic implementation provides a compact and programmable platform realizing, to our knowledge, multistability governed by coupling nonlinearity.

Our nonlinear coupling mechanism fundamentally differs from Kerr-type nonlinear systems, where increasing drive strength typically induces direct LS → IS transfers when the intermediate state exists [21]. In our system, the sign-flipping nature of the nonlinear coupling is pivotal for achieving tristability; otherwise, the system degenerates to conventional bistability (see Sec. 4.2 in [40] for the case of $\kappa_0 = 0$, i.e., purely nonlinear coupling). In addition, the sign-flipping process of κ occurs when $|\kappa| \approx 0$, a condition that coincides with the IS and remarkably decouples the two resonators. This dynamical decoupling suppresses energy transfer between cavities, leading to strongly asymmetric wave responses (see Sec. 4.1 in [40] for experimental measurements in both resonators).

The approach is readily extensible. More general coupling laws—$\kappa(|\psi_1|^2, |\psi_2|^2)$, saturable or nonlocal forms, time-modulated or non-Hermitian interactions, and network/array geometries—are expected to produce analogous basin-mediated selection rules and additional classes of hidden states. Our findings, together with other recent explorations of nonlinear coupling in diverse platforms such as circuit systems for non-Hermitian physics [37], underscore the broad potential of this paradigm. We anticipate that these ideas can be transferred to diverse platforms, enabling programmable multistate memory and nonlinear signal processing, and offering a route to explore coupling-driven phenomena at the frontier of nonlinear dynamics [52–57].

Note added—Recently, we became aware of a related preprint that excites fully hidden states through Kerr nonlinearity and pulsed excitation [58]. In contrast, our scheme employs coupling nonlinearity and adiabatic drive modulation to engineer the basins of attraction.

Acknowledgments—This work was supported by the National Key R&D Program of China (Grants No. 2023YFA1406900 and No. 2022YFA1405000), the National Natural Science Foundation of China (Grants No. 12474154 and No. 12404506), and Natural Science Foundation of Jiangsu Province, Major Project (No. BK20243067).

Data availability—The data that support the findings of this article are not publicly available. The data are available from the authors upon reasonable request.

[1] U. Feudel, Complex dynamics in multistable systems, Int. J. Bifurcation Chaos Appl. Sci. Eng. **18**, 1607 (2008).
[2] A. N. Pisarchik and U. Feudel, Control of multistability, Phys. Rep. **540**, 167 (2014).
[3] S. H. Strogatz, *Nonlinear Dynamics and Chaos: With Applications to Physics, Biology, Chemistry, and Engineering* (Chapman and Hall/CRC, London, 2024).
[4] V. Kubytskyi, S.-A. Biehs, and P. Ben-Abdallah, Radiative bistability and thermal memory, Phys. Rev. Lett. **113**, 074301 (2014).
[5] H. Yasuda and J. Yang, Reentrant origami-based metamaterials with negative Poisson's ratio and bistability, Phys. Rev. Lett. **114**, 185502 (2015).
[6] Y.-P. Wang, G.-Q. Zhang, D. Zhang, T.-F. Li, C.-M. Hu, and J. Q. You, Bistability of cavity magnon polaritons, Phys. Rev. Lett. **120**, 057202 (2018).
[7] M. X. Bi, X. H. Yan, Y. Zhang, and Y. Xiao, Tristability of cavity magnon polaritons, Phys. Rev. B **103**, 104411 (2021).

[8] R.-C. Shen, J. Li, Z.-Y. Fan, Y.-P. Wang, and J. Q. You, Mechanical bistability in Kerr-modified cavity magnomechanics, Phys. Rev. Lett. **129**, 123601 (2022).
[9] R. Xu, C. Linghu, W. Mao, H. Zhang, H. Jiang, Y. He, Y. Liu, Y. Li, H. Gao, Y.-F. Chen, M.-H. Lu, X. Li, and K. J. Hsia, Shape-adaptive mechanical metastructure enables robust adhesion and dynamic capturing of 3d objects, Adv. Funct. Mater. e14499 (2025).
[10] J. A. S. Kelso, Multistability and metastability: Understanding dynamic coordination in the brain, Phil. Trans. R. Soc. B **367**, 906 (2012).
[11] L.-Z. Wang, R.-Q. Su, Z.-G. Huang, X. Wang, W.-X. Wang, C. Grebogi, and Y.-C. Lai, A geometrical approach to control and controllability of nonlinear dynamical networks, Nat. Commun. **7**, 11323 (2016).
[12] B. Huang, Y. Xia, F. Liu, and W. Wang, Realization of tristability in a multiplicatively coupled dual-loop genetic network, Sci. Rep. **6**, 28096 (2016).
[13] Y. Tadokoro and H. Tanaka, Highly sensitive implementation of logic gates with a nonlinear nanomechanical resonator, Phys. Rev. Appl. **15**, 024058 (2021).
[14] R.-C. Shen, Y.-P. Wang, J. Li, S.-Y. Zhu, G. S. Agarwal, and J. Q. You, Long-time memory and ternary logic gate using a multistable cavity magnonic system, Phys. Rev. Lett. **127**, 183202 (2021).
[15] R. Fermin, N. M. A. Scheinowitz, J. Aarts, and K. Lahabi, Mesoscopic superconducting memory based on bistable magnetic textures, Phys. Rev. Res. **4**, 033136 (2022).
[16] J.-S. Kim, C.-S. Ri, Y.-J. Yun, S.-J. Im, K.-D. Kim, K.-S. Song, J.-S. Pae, and K.-S. Ho, On-chip deep subwavelength optomagnetic bistable memory based on inverse Faraday effect related nonlinearity in graphene waveguide ring resonators, Phys. Rev. B **110**, 195421 (2024).
[17] M. Hirota, M. Holmgren, E. H. V. Nes, and M. Scheffer, Global resilience of tropical forest and savanna to critical transitions, Science **334**, 232 (2011).
[18] A. L. Zerkle, M. W. Claire, S. D. Domagal-Goldman, J. Farquhar, and S. W. Poulton, A bistable organic-rich atmosphere on the Neoarchaean earth, Nat. Geosci. **5**, 359 (2012).
[19] L. De Mot, D. Gonze, S. Bessonnard, C. Chazaud, A. Goldbeter, and G. Dupont, Cell fate specification based on tristability in the inner cell mass of mouse blastocysts, Biophys. J. **110**, 710 (2016).
[20] Y. Ma, B. Liu, L.-H. Zhang, Y.-J. Wang, Z.-Y. Zhang, S.-Y. Shao, Q. Li, H.-C. Chen, J. Zhang, T.-Y. Han, Q.-F. Wang, J.-D. Nan, Y.-M. Yin, D.-Y. Zhu, B.-S. Shi, and D.-S. Ding, Folded multistability and hidden critical point in microwave-driven Rydberg atoms, arXiv:2408.10514.
[21] M.-X. Bi, H. Fan, X.-H. Yan, and Y.-C. Lai, Folding state within a hysteresis loop: Hidden multistability in nonlinear physical systems, Phys. Rev. Lett. **132**, 137201 (2024).
[22] D. Smirnova, D. Leykam, Y. Chong, and Y. Kivshar, Nonlinear topological photonics, Appl. Phys. Rev. **7**, 021306 (2020).
[23] Y. Ota, K. Takata, T. Ozawa, A. Amo, Z. Jia, B. Kante, M. Notomi, Y. Arakawa, and S. Iwamoto, Active topological photonics, Nanophotonics **9**, 547 (2020).
[24] S. Mukherjee and M. C. Rechtsman, Observation of Floquet solitons in a topological bandgap, Science **368**, 856 (2020).
[25] S. Xia, D. Kaltsas, D. Song, I. Komis, J. Xu, A. Szameit, H. Buljan, K. G. Makris, and Z. Chen, Nonlinear tuning of PT symmetry and non-Hermitian topological states, Science **372**, 72 (2021).
[26] M. S. Kirsch, Y. Zhang, M. Kremer, L. J. Maczewsky, S. K. Ivanov, Y. V. Kartashov, L. Torner, D. Bauer, Alexander, and M. Heinrich, Nonlinear second-order photonic topological insulators, Nat. Phys. **17**, 995 (2021).
[27] M. Juergensen, S. Mukherjee, and M. Rechtsman, Quantized nonlinear Thouless pumping, Nature (London) **596**, 63 (2021).
[28] A. Szameit and M. C. Rechtsman, Discrete nonlinear topological photonics, Nat. Phys. **20**, 195421 (2024).
[29] K. Bai, C. Lin, T. Liu, J.-Z. Li, X. Lyu, and M. Xiao, Nonlinear chiral-like state transfer realized with a minimal set of parameters, Nat. Commun. **16**, 5844 (2025).
[30] Y. Hadad, A. B. Khanikaev, and A. Alù, Self-induced topological transitions and edge states supported by nonlinear staggered potentials, Phys. Rev. B **93**, 155112 (2016).
[31] Y. Hadad, J. C. Soric, A. B. Khanikaev, and A. Alù, Self-induced topological protection in nonlinear circuit arrays, Natl. Electron. Rev. **1**, 178 (2018).
[32] F. Zangeneh-Nejad and R. Fleury, Nonlinear second-order topological insulators, Phys. Rev. Lett. **123**, 053902 (2019).
[33] L. J. Maczewsky, M. Heinrich, M. Kremer, S. K. Ivanov, M. Ehrhardt, F. Martinez, Y. V. Kartashov, V. V. Konotop, L. Torner, D. Bauer, and A. Szameit, Nonlinearity-induced photonic topological insulator, Science **370**, 701 (2020).
[34] D. Zhou, D. Z. Rocklin, M. Leamy, and Y. Yao, Topological invariant and anomalous edge modes of strongly nonlinear systems, Nat. Commun. **13**, 3379 (2022).
[35] K. Sone, M. Ezawa, Y. Ashida, N. Yoshioka, and T. Sagawa, Nonlinearity-induced topological phase transition characterized by the nonlinear Chern number, Nat. Phys. **20**, 195421 (2024).
[36] K. Sone, M. Ezawa, Z. Gong, T. Sawada, N. Yoshioka, and T. Sagawa, Transition from the topological to the chaotic in the nonlinear Su–Schrieffer–Heeger model, Nat. Commun. **16**, 422 (2025).
[37] J. Wu, R.-C. Shen, L. Zhang, F. Chen, B. Wang, H. Chen, Y. Yang, and H. Xue, Observation of localization reversal and harmonic generation in nonlinear non-Hermitian skin effect, arXiv:2505.09179.
[38] H. Haus and W. Huang, Coupled-mode theory, Proc. IEEE **79**, 1505 (1991).
[39] Z.-X. Chen, W.-G. Song, G.-C. He, X.-M. Zhang, Z.-G. Chen, H. Xu, and E. Prodan, Emulation of Schrödinger dynamics with metamaterials, Sci. Bull. **70**, 1347 (2025).
[40] See Supplemental Material at http://link.aps.org/supplemental/10.1103/6bsr-x2v9, which includes Refs. [41,42], for more details about the theoretical design, experimental setup, coupled mode theory, and more experimental results.
[41] B. Sendov, A. Andreev, and N. Kyurkchiev, Numerical solution of polynomial equations, in *Handbook of Numerical Analysis* (Elsevier, Amsterdam, 1994), Vol. 3, p. 625.
[42] O. Balabanov and L. Grigori, Randomized Gram–Schmidt process with application to GMRES, SIAM J. Sci. Comput. **44**, A1450 (2022).

[43] R. Muolo, A. Hastir, and H. Nakao, Stabilization of hyperbolic reaction-diffusion systems on directed networks through the generalized Routh-Hurwitz criterion for complex polynomials, in *2024 SICE International Symposium on Control Systems (SICE ISCS)* (IEEE, New York, 2024), pp. 73–79.

[44] L. Zhang, Y. Yang, Y. Ge *et al.*, Acoustic non-Hermitian skin effect from twisted winding topology, Nat. Commun. **12**, 6297 (2021).

[45] J.-J. Liu, Z.-w. Li, Z.-G. Chen, W. Tang, A. Chen, B. Liang, G. Ma, and J.-C. Cheng, Experimental realization of Weyl exceptional rings in a synthetic three-dimensional non-Hermitian phononic crystal, Phys. Rev. Lett. **129**, 084301 (2022).

[46] Q. Zhang, Y. Li, H. Sun, X. Liu, L. Zhao, X. Feng, X. Fan, and C. Qiu, Observation of acoustic non-Hermitian Bloch braids and associated topological phase transitions, Phys. Rev. Lett. **130**, 017201 (2023).

[47] Z.-X. Chen, A. Chen, Y.-G. Peng, Z.-w. Li, B. Liang, J. Yang, X.-F. Zhu, Y.-q. Lu, and J.-c. Cheng, Observation of acoustic Floquet π modes in a time-varying lattice, Phys. Rev. B **109**, L020302 (2024).

[48] S. Tong, Q. Zhang, L. Qi, G. Li, X. Feng, and C. Qiu, Observation of Floquet-Bloch braids in non-Hermitian spatiotemporal lattices, Phys. Rev. Lett. **134**, 126603 (2025).

[49] Z.-X. Chen, Y.-H. Zhang, X.-C. Sun, R.-Y. Zhang, J.-S. Tang, X. Yang, X.-F. Zhu, and Y.-Q. Lu, Direct measurement of topological invariants through temporal adiabatic evolution of bulk states in the synthetic Brillouin zone, Phys. Rev. Lett. **134**, 136601 (2025).

[50] R. Xu, C. Chen, J. Sun, Y. He, X. Li, M.-H. Lu, and Y. Chen, The design, manufacture and application of multistable mechanical metamaterials-a state-of-the-art review, Int. J. Extrem. Manuf. **5**, 042013 (2023).

[51] N. Gao, T. Ma, Y. Wang, W. Zhou, Y.-S. Wang, and W. Chen, A brief review of solitary waves in nonlinear metamaterials, Mech. Res. Commun. **137**, 104260 (2024).

[52] Q. Fu, P. Wang, Y. V. Kartashov, V. V. Konotop, and F. Ye, Nonlinear Thouless pumping: Solitons and transport breakdown, Phys. Rev. Lett. **128**, 154101 (2022).

[53] N. Pernet, P. St-Jean, D. D. Solnyshkov, G. Malpuech, N. Carlon Zambon, Q. Fontaine, B. Real, O. Jamadi, A. Lemaître, M. Morassi *et al.*, Gap solitons in a one-dimensional driven-dissipative topological lattice, Nat. Phys. **18**, 678 (2022).

[54] Y. Pan, M.-I. Cohen, and M. Segev, Superluminal k-gap solitons in nonlinear photonic time crystals, Phys. Rev. Lett. **130**, 233801 (2023).

[55] K. Bai, J.-Z. Li, T.-R. Liu, L. Fang, D. Wan, and M. Xiao, Nonlinear exceptional points with a complete basis in dynamics, Phys. Rev. Lett. **130**, 266901 (2023).

[56] J. Veenstra, O. Gamayun, X. Guo, A. Sarvi, C. V. Meinersen, and C. Coulais, Non-reciprocal topological solitons in active metamaterials, Nature (London) **627**, 528 (2024).

[57] W. Zhang, F. Di, and X. Zhang, Non-Hermitian global synchronization, Adv. Sci. **12**, 2408460 (2025).

[58] K. Zhang, Q. Zhang, S. Tong, W. Wu, X. Feng, and C. Qiu, preceding Letter, Experimental observation of hidden multistability in nonlinear systems, Phys. Rev. Lett. **136**, 037201 (2026).